# Latitudinal Structure of the Meridional Overturning Circulation Variability on Interannual to Decadal Time Scales in the North Atlantic Ocean

SIJIA ZOU[a] AND M. SUSAN LOZIER

*Duke University, Durham, North Carolina*

XIAOBIAO XU

*Center for Ocean–Atmospheric Prediction Studies, Florida State University, Tallahassee, Florida*

(Manuscript received 22 March 2019, in final form 31 January 2020)

ABSTRACT

The latitudinal structure of the Atlantic meridional overturning circulation (AMOC) variability in the North Atlantic is investigated using numerical results from three ocean circulation simulations over the past four to five decades. We show that AMOC variability south of the Labrador Sea (53°N) to 25°N can be decomposed into a latitudinally coherent component and a gyre-opposing component. The latitudinally coherent component contains both decadal and interannual variabilities. The coherent decadal AMOC variability originates in the subpolar region and is reflected by the zonal density gradient in that basin. It is further shown to be linked to persistent North Atlantic Oscillation (NAO) conditions in all three models. The interannual AMOC variability contained in the latitudinally coherent component is shown to be driven by westerlies in the transition region between the subpolar and the subtropical gyre (40°–50°N), through significant responses in Ekman transport. Finally, the gyre-opposing component principally varies on interannual time scales and responds to local wind variability related to the annual NAO. The contribution of these components to the total AMOC variability is latitude-dependent: 1) in the subpolar region, all models show that the latitudinally coherent component dominates AMOC variability on interannual to decadal time scales, with little contribution from the gyre-opposing component, and 2) in the subtropical region, the gyre-opposing component explains a majority of the interannual AMOC variability in two models, while in the other model, the contributions from the coherent and the gyre-opposing components are comparable. These results provide a quantitative decomposition of AMOC variability across latitudes and shed light on the linkage between different AMOC variability components and atmospheric forcing mechanisms.

## 1. Introduction

The upper limb of the Atlantic meridional overturning circulation (AMOC) transports warm, saline waters northward in the upper layer to the subpolar/subarctic North Atlantic, where they are transformed into cold, fresh waters that flow southward in the deep limb. Due to its role in redistributing heat, freshwater, and carbon, the AMOC and its variability have significant impacts on the Earth climate system, including European climate (Stouffer et al. 2006), North Atlantic hurricane activity (Zhang and Delworth 2006), and regional sea level (Pardaens et al. 2011; Little et al. 2017).

The forcing mechanisms for AMOC variability are believed to be time-scale dependent. On interannual time scales, both observational and modeling studies have shown the AMOC to be primarily wind driven. For example, the observed interannual AMOC variability at 26.5°N is dominated by wind-driven Ekman transport and upper midocean transport (e.g., McCarthy et al. 2012). Modeling studies have indicated that this high-frequency wind-dominant AMOC variability is also

Denotes content that is immediately available upon publication as open access.

Supplemental information related to this paper is available at the Journals Online website: https://doi.org/10.1175/JCLI-D-19-0215.s1.

[a] Current affiliation: Woods Hole Oceanographic Institution, Woods Hole, Massachusetts.

*Corresponding author*: Sijia Zou, szou@whoi.edu

DOI: 10.1175/JCLI-D-19-0215.1

present at other latitudes in the North Atlantic (e.g., Biastoch et al. 2008; Xu et al. 2014; Yeager and Danabasoglu 2014; Zhao 2017). On the decadal time scale, modeling results indicate that AMOC variability is linked to the production of Labrador Sea Water, which varies according to the local buoyancy forcing in that basin (Delworth et al. 1993; Böning et al. 2006; Biastoch et al. 2008; Xu et al. 2013). As such, it has been proposed that changes in density and/or sea surface height in the Labrador Sea can be used as skillful indicators and predictors of AMOC decadal variability (e.g., Yeager and Danabasoglu 2014; Robson et al. 2016).

A number of modeling studies have indicated that the meridional coherence of AMOC also depends on time scales. Subpolar-originated decadal AMOC anomalies have been shown to propagate downstream from the subpolar to the subtropical regions through boundary waves (Häkkinen 1999; Biastoch et al. 2008; Eden and Willebrand 2001; Johnson and Marshall 2002; Marshall and Johnson 2013), advective processes (Marotzke and Klinger 2000; Buckley et al. 2012), or both (Getzlaff et al. 2005; Zhang 2010), thereby producing coherent decadal AMOC variability across a number of latitudes. A more quantitative description of the coherent decadal AMOC variability is provided in several modeling studies by applying empirical orthogonal function (EOF) analysis on the overturning streamfunction. For example, in a coupled atmosphere–ocean model, Bingham et al. (2007) applied EOF analysis on the overturning streamfunction over a 100-yr period and found that the leading mode (explaining 25% of the variance) captured the meridionally coherent AMOC variability. This mode, primarily varying on decadal time scales, is most vigorous north of 40°N and decays southward. Similar results were found by Yeager and Danabasoglu (2014) and Danabasoglu et al. (2012) with ocean–sea ice fully coupled models, yet these studies had a larger percentage (38% and 69%, respectively) for the explained variance.

The meridional coherence of AMOC, however, breaks down between the subpolar and the subtropical regions on interannual time scales. The meridional heat transports inferred from observations (Kelly et al. 2014) and the AMOC transports based on a high-resolution model (Xu et al. 2014) both show a meridionally coherent variability south of 35°–40°N, but not to the north. A similar breakdown of the AMOC meridional coherence can be found in Biastoch et al. (2008) and Yeager and Danabasoglu (2014) when high-frequency wind forcing is introduced. As a consequence, the EOF structure of AMOC variability on these shorter time scales is quite different from that on decadal time scales. With an ocean reanalysis, Cabanes et al. (2008) found that the dominant EOF mode (68%) for interannual to semidecadal (3–10 years) AMOC variability during 1993–2003 is concentrated in the subtropical region (~25°N). This mode is shown to be linked to the wind variability associated with the North Atlantic Oscillation (NAO).

Taken together, these studies suggest that the AMOC strength at a specific latitude in the North Atlantic contains a decadal component that originates in the subpolar region in response to surface buoyancy flux in the Labrador Sea, and an interannual component driven by local wind variability. However, recent studies and observations have raised questions about this paradigm. First, a direct linkage between Labrador Sea buoyancy flux and AMOC variability has not been established. Using summer hydrographic data from the 1990s, Pickart and Spall (2007) suggested that overturning (i.e., diapycnal transformation) in the Labrador Sea contributed only ~2 Sv ($1\,\mathrm{Sv} \equiv 10^6\,\mathrm{m^3\,s^{-1}}$) to the overall AMOC measure. This finding was recently confirmed by a more substantial observational effort in the subpolar North Atlantic (Lozier et al. 2019). Moreover, using a suite of ocean–sea ice models, a recent study found no consistency among models in the relationship between the production of Labrador Sea Water and the AMOC variability across latitudes (Li et al. 2019). Second, the role of winds simply as a disruptor of meridional coherence may be oversimplified. For example, the modeling study of Polo et al. (2014) suggested that interannual to decadal AMOC variability at 26°N can be impacted by winds at 40°N. With observed time series from 2004 to 2008, Elipot et al. (2017) showed that basin-scale wind stress was responsible for the coherent AMOC variability across four latitudes (42.5°, 39°, 26.5°, and 16°N). Furthermore, a recent modeling study by Zou et al. (2019) showed a possible connection between cumulative NAO forcing in the subpolar region and individual NAO forcing (primarily wind forcing) in the subtropical region, which can create an apparent linkage of AMOC variability across different latitudes during certain periods (e.g., the 1990s). These studies suggest that instead of simply disrupting meridional coherence, winds might contribute to a larger coherent pattern of AMOC variability.

In addition, the EOF-based decomposition of AMOC variability is not fully understood. First, there is a lack of knowledge on the relative importance of the meridionally coherent and the localized components of AMOC variability at different latitudes. For example, even though the meridionally coherent component is present at the subtropical latitudes, it may not contribute significantly to the local AMOC variability, even on decadal time scales. Indeed, Lozier et al. (2010) found that the decadal change of subtropical AMOC between 1950–70 and 1980–2000 opposed the decadal change of

the subpolar AMOC, highlighting the importance of gyre-specific dynamics on the overturning variability. Second, the mechanistical linkage of the decomposed AMOC variability to different forcing is not completely addressed. Last, but not least, most previous studies have calculated AMOC in depth space, which represents the vertical sinking of waters but not necessarily the total diapycnal transformation rate. Specifically, in the subpolar region, where isopycnal surfaces are significantly tilted across the basin (e.g., Zhang 2010; Lozier et al. 2019; Xu et al. 2014), such calculations lead to an underestimation of the mean and variability of the AMOC, and may influence the EOF-based decomposition of AMOC variability.

In light of these recent studies and the knowledge gaps, the goal of this work is to re-examine the meridional structure of the AMOC variability in density space from interannual to decadal time scales and to investigate the associated atmospheric forcing mechanisms. With this study, we aim to provide a mechanistically linked quantitative decomposition of AMOC variability across latitudes in the North Atlantic.

## 2. Numerical simulations and methods

### a. Numerical simulations

In an effort to test robustness across modeling frameworks, we use numerical outputs from three simulations based on different ocean general circulation models (OGCMs) and different model configurations for our study. For all models, we focus our study on the latitudes south of the exit of the Labrador Sea (53°N) in order to investigate AMOC meridional coherence downstream of the convective basins. A preliminary extension of this analysis farther north (e.g., 60°N) revealed significant differences among models in terms of AMOC variability, especially on interannual time scales. These differences may result from specific model configurations, such as the representation of dense Nordic seas overflows, that differentially impact the high-latitude AMOC. Since model results are largely consistent south of 53°N (as shown in the following sections), this paper finds its focus there.

#### 1) SODA3.4.2

The Simple Ocean Data Assimilation ocean/sea ice reanalysis (SODA, version 3.4.2) is based on the GFDL MOM5/SIS1 model, with an eddy-permitting horizontal resolution of 1/4° (28 km at the equator and 10 km at polar latitudes) and 50 vertical levels (Carton et al. 2018). The model is forced with European Centre for Medium-Range Weather Forecasts (ECMWF) interim reanalysis (ERA-Interim) and uses the COARE4 bulk formula. Observations from World Ocean Database (WOD) and the International Comprehensive Ocean–Atmosphere Dataset (ICOADS) are sequentially assimilated in SODA (Carton and Giese 2008). It is noted here that SODA directly modifies the model fields with observations and is therefore not dynamically consistent, which is different from the other two models used in this study.

The SODA outputs used in this paper are the monthly averages mapped onto a uniform 0.5° × 0.5° 50-level grid from 1980 to 2015. While transports should ideally be calculated using variables on the native model grid, these fields are not fully available for SODA3.4.2. However, analyses with the two other models used in this study show that interpolation errors mainly affect transport magnitude and have less of an impact on transport variability, which is the focus here. The simulated AMOC variability at 26°N in SODA3.4.2 compares well with the observed variability of the annual mean AMOC transport at 26.5°N (from RAPID) from 2004 to 2015 (correlation coefficient $r = 0.67$).

#### 2) ORCA025

ORCA025 is a nonassimilating global ocean/sea ice model based on the Nucleus for European Modelling of the Ocean (NEMO) system (Barnier et al. 2006, 2007). The model is implemented on a quasi-isotropic tripolar grid and has an eddy-permitting horizontal resolution of 1/4°. It has 46 vertical levels, with spacing increasing from 6 m near the surface to a maximum of 250 m near the bottom. The model is forced with the European Remote Sensing Satellite (ERS) scatterometer data and NCEP–NCAR reanalysis data, with an empirical bulk parameterization applied for surface fluxes (Goosse 1997). Further details and model validations can be found in Barnier et al. (2006), Gary et al. (2011), and Zou and Lozier (2016). The monthly mean outputs from 1961 to 2004 are used in this study.

#### 3) HYCOM

Finally, we use model outputs from an Atlantic simulation of the Hybrid Coordinate Ocean Model (HYCOM). This basin-scale simulation, also not data assimilated, has a computational domain from 30°S to 80°N, with a horizontal resolution of 1/12° and vertical resolution of 32 layers in $\sigma_2$. The simulation is initialized from a 10-yr climatological spinup and is integrated using a combination of three atmospheric forcing products to cover a time period of 1978–2015: the ECMWF 40-yr reanalysis (ERA-40; Uppala et al. 2005) for 1978–2002; the Navy Operational Global Atmospheric Prediction System (NOGAPS; Rosmond et al. 2002) for 2003–12, and NOGAPS's successor, the Navy Global Environmental Model (NAVGEM), for 2013–15. The

reader is referred to Xu et al. (2013) for further configuration details. Clearly, the combination of different forcing products (based on different models, resolutions, and data assimilation methods) is not ideal because it could introduce unrealistic discontinuity into the forcing, to which the ocean responds. The correlation coefficient ($r = 0.45$) between the observed and modeled annual mean AMOC transports at 26.5°N is lower than that of the SODA. However, the simulation is shown to reproduce the observed warming and sea surface height variability in the central Labrador Sea and the associated change in the strength of the western boundary current in the subpolar North Atlantic (Xu et al. 2013). The simulation also represents well the observed variability of the westward Iceland–Scotland Overflow Water transports through key locations such as the Charlie Gibbs Fracture Zone (Xu et al. 2018a). The monthly mean model outputs from 1978 to 2015 are used in this study.

### b. Calculating AMOC in density coordinates

As stated above, both the mean and variability of the AMOC defined in depth space can be greatly underestimated at higher latitudes due to significantly sloped isopycnals. As a result, we define the AMOC in density coordinate in all three models: at each latitude $\varphi$, AMOC strength is defined as the maximum of the overturning streamfunction $\Psi$ that is integrated from $\sigma_{2\text{surface}} = 30\,\text{kg m}^{-3}$ to a density level $\sigma_2$ (with reference to 2000 dbar):

$$\begin{aligned}\text{AMOC}(\varphi, t) &= \max\Psi(\varphi, \sigma_2, t)\\ &= \max\left[\int_{\sigma_{2\text{surface}}}^{\sigma_2}\int_{x_w}^{x_e} v(x, \varphi, \sigma_2, t)\,dx\,d\sigma_2\right].\end{aligned}$$

Here, $v(x, \varphi, \sigma_2, t)$ is the meridional velocity in $\sigma_2$ space and $x$ is distance, with $x_w$ and $x_e$ denoting the westernmost and easternmost positions of the ocean bottom at a particular $\sigma_2$ level, respectively. The AMOC strength, AMOC($\varphi$, $t$), achieved at $\sigma_2 = \sigma_2^{\max}(\varphi, t)$, is calculated from monthly output at each latitude south of the exit of the Labrador Sea (53°N), to near the southern limit of the subtropical region (25°N). Monthly AMOC values are averaged annually and then a linear trend is removed over the time period for each model. Calculations of AMOC transport in other density coordinates (e.g., $\sigma_0$ with reference to the surface and neutral density) yield similar results.

Figures 1a–c show the mean overturning streamfunction in density space for each model. In all three simulations, there exist 1) a weak overturning cell in shallow waters ($\leq 35\,\text{kg m}^{-3}$) south of 35°N, representing the diapycnal transformation associated with the subtropical gyre (Xu et al. 2016, 2018b), and 2) a stronger overturning cell between 36 and $37\,\text{kg m}^{-3}$ across all latitudes, representing the diapycnal transformation associated with the basin-scale AMOC. The time-mean AMOC($\varphi$) generally increases from subtropical to subpolar latitudes. In SODA, AMOC strength is maximized at ~40°N, where it is 23 Sv. In ORCA and HYCOM, the strongest AMOC is found at 53°N, with means of 16 Sv for ORCA and 22 Sv for HYCOM. In addition to a larger mean transport, AMOC variability is also stronger in SODA than that in the other two models (Figs. 1d–f). The standard deviation (STD) for annual mean AMOC transports in SODA ranges from 2 to 4 Sv across all latitudes, with a maximum at 41°N. For comparison, the STD values for the annual mean AMOC transports are 0.9–1.3 Sv in ORCA and 1.0–2.0 Sv in HYCOM.

Despite these differences in mean AMOC transports and the STD of the AMOC variability, we show in the next section that there is consistency across these models in the meridional structure of the AMOC variability, as well as with the atmospheric forcing associated with each component of variability.

## 3. Results

### a. Decomposing AMOC variability

The modeled AMOC variability at different latitudes is decomposed with EOF analysis. Figure 2 shows the spatial structures of the first two EOF modes, which explain a majority (73%–84%) of the total variance and are therefore the focus of this study. The first EOF mode (EOF1) explains 46%–63% of the variance and it exhibits consistent AMOC variability from 25° to 53°N in all three models (Fig. 2a). As such, it is referred to as the meridionally coherent mode. This mode is generally stronger at subpolar latitudes and gradually decreases in strength toward the subtropical latitudes. Frequency analysis on the first principal component time series (PC1) shows that this coherent mode contains both high-frequency (interannual) and low-frequency (semidecadal to decadal) variability. Despite the differences in magnitude, the low-frequency variability exhibits a similar phase between SODA and HYCOM (Fig. 3): both show a weaker AMOC in the 1980s and the strongest AMOC in the 1990s. In ORCA, the decadal changes of AMOC in the 1980s and 1990s are also present, but are much less significant compared to the other two models. The second EOF mode (EOF2) explains 16%–27% of the total variance and exhibits an opposing AMOC variability between the subpolar and subtropical regions (Fig. 2b). This

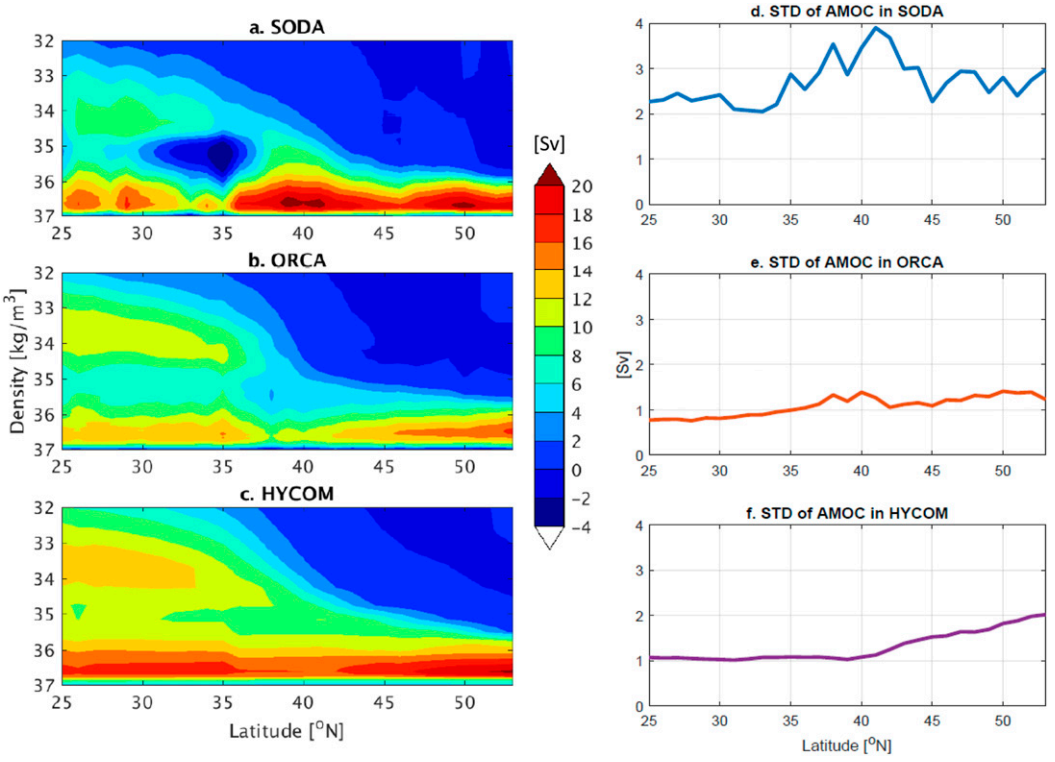


FIG. 1. (left) Mean overturning streamfunction as a function of latitude and density, based on (a) 1/4° SODA (1980–2015), (b) 1/4° ORCA025 (1961–2004), and (c) 1/12° HYCOM (1978–2015). Density is referenced to 2000 dbar. (right) Standard deviation (STD) of annual AMOC time series at each latitude in (d) SODA, (e) ORCA, and (f) HYCOM.

mode is referred to as the gyre-opposing mode. The mode is dominated by interannual variability (Figs. 3d–f) and shows no significant variability on longer (e.g., decadal) time scales according to frequency analysis (not shown).

The contribution of the two EOF modes to the AMOC variability is latitude-dependent and model-dependent. Here we show examples at three different latitudes in each model (Fig. 4). At 30°N in SODA, the reconstructed AMOC variability from the EOF1 mode and from the EOF2 mode contribute equally (~41%) to the total AMOC variability (Fig. 4a). In ORCA and HYCOM, on the other hand, over 70% of AMOC variability can be reconstructed with EOF2 mode alone, with a small or no contribution from EOF1 mode (Figs. 4d,g). At certain latitudes (40°N in SODA, 43°N in ORCA, and 42°N in HYCOM), EOF2 mode has zero magnitude (Fig. 2b). AMOC variability at these latitudes primarily reflects EOF1 mode (73%–80%) with no contribution from EOF2 mode (Figs. 4b,e,h). As these latitudes are generally located near the boundary between the subpolar and the subtropical region and they specify where EOF2 mode reverses its sign, we refer to these latitudes as the transition latitudes. Note that these transition latitudes do not represent the dynamic boundary between the subpolar and the subtropical gyre, which is determined by the wind pattern. From the transition latitudes to ~50°N, the contribution from EOF2 mode increases, but is still small compared to that from EOF1 mode (Figs. 4c,f,i).

The contribution percentages of the two EOF modes to AMOC variability at other latitudes are shown in Fig. 5. In general, north of ~43°N, AMOC variability is dominated by EOF1 mode in all three models, contributing 60%–90% to the total. The contribution from EOF2 mode is quite small (<16%), but can be significant at certain latitudes. In the subtropical region (south of 35°N), AMOC variability is dominated by EOF2 mode (50%–85%) in ORCA and HYCOM, with a negligible/weak contribution from EOF1 mode. In SODA, however, the contribution from EOF2 mode is comparable to that from EOF1 mode, especially south of 30°N where both modes contribute 35%–50%. This suggests a stronger meridional connection of AMOC variability in SODA. The sum of EOF1 and EOF2 modes explains a significant percentage of total AMOC variability at most of the latitudes. However, these

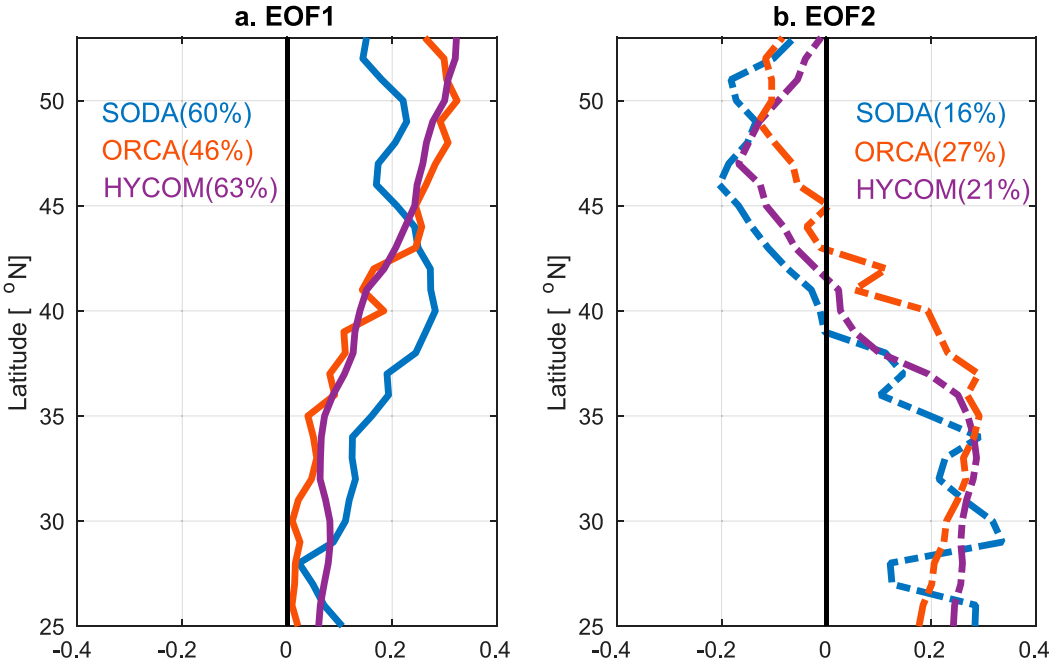


FIG. 2. (a) EOF1 mode and (b) EOF2 mode of the annual AMOC transports as a function of latitude in three models.

modes fail to capture a large fraction of the AMOC variability at 37°–42°N in ORCA and HYCOM (Figs. 5b,c). At these latitudes, the substantial variability of the Gulf Stream, in both transport and position, may introduce local AMOC anomalies that are not captured by the latitudinal EOF modes.

In summary, we have decomposed the AMOC variability at different latitudes into a meridionally coherent

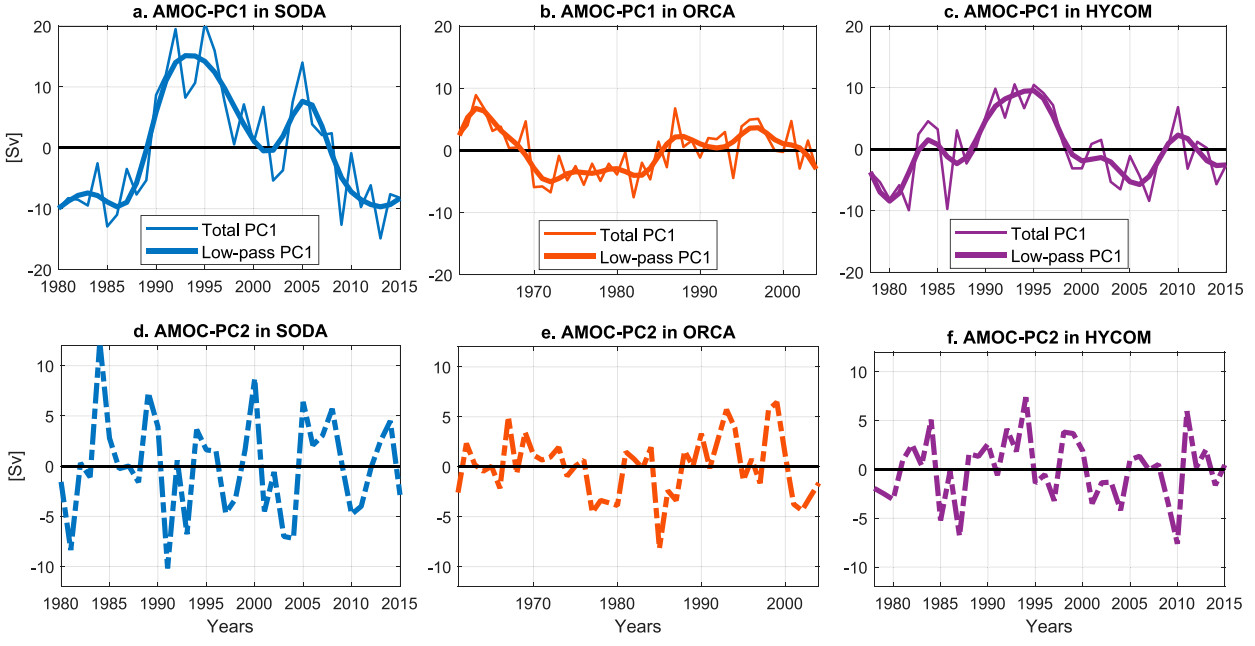


FIG. 3. (a)–(c) Time series of AMOC-PC1. Thin lines represent the original PC1 time series, and the thick lines represent the low-pass-filtered time series obtained by applying a fifth-order Butterworth low-pass filter with a cutoff period of 3 years. (d)–(f) As in (a)–(c), but for PC2. Note that one needs to multiply the PC time series with the EOF to get the associated AMOC variability.

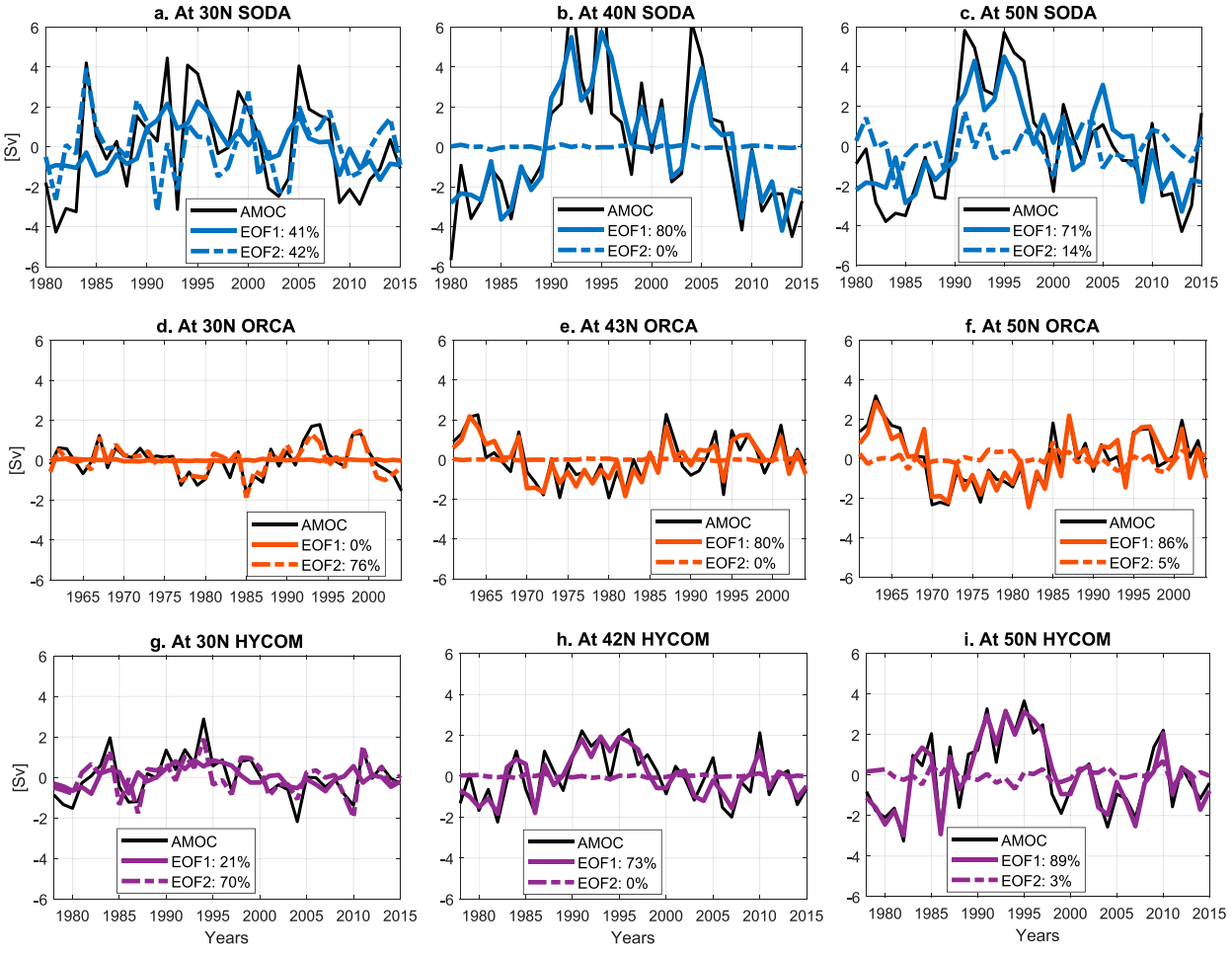


FIG. 4. (left) Time series of AMOC (black) at 30°N in (a) SODA, (d) ORCA, and (g) HYCOM. AMOC reconstructed from EOF1 mode (EOF2 mode) is shown as a colored solid (dashed) line. The contribution percentage for each EOF mode is calculated as $r^2 \times 100\%$, where $r$ is the correlation coefficient between the reconstructed AMOC from each mode and the total AMOC variability. (center) As in the left column, but at the transition latitude. The transition latitude, (b) 40°N in SODA, (e) 43°N in ORCA, and (h) 42°N in HYCOM, is defined by where the EOF2 mode has no contribution to the total AMOC. (right) As in the left column, but at 50°N.

mode and a gyre-opposing mode. The coherent mode dominates AMOC variability in the subpolar region in all three models. The gyre-opposing mode dominates AMOC variability in the subtropical region in ORCA and HYCOM. In SODA, both modes contribute to the subtropical AMOC variability. It should be noted that the EOF analysis does not consider lagged connectivity of AMOC variability between the subpolar and the subtropical gyre. Lagged AMOC connectivity can result from two scenarios: 1) a real connectivity in response to a specified forcing and 2) an "apparent" connectivity created by gyre-specific forcing scenarios (Zou et al. 2019). As for scenario 1, the "static" EOF analysis may lead to an underestimation of the coherent AMOC mode at the subtropical latitudes if lags are not considered. However, given the significant difference in varying time scales (decadal vs interannual) and forcing mechanism (cumulative NAO vs annual NAO; see section 3b) of the AMOC between the subpolar gyre and the subtropical gyre, we believe the underestimation is small. As for the second scenario, which Zou et al. (2019) consider to be more likely, EOF analysis helps to disentangle the forcing that drives the meridionally coherent AMOC mode from that drives the gyre-opposing mode.

### b. *Atmospheric forcing linked to AMOC variability*

We next diagnose forcing mechanisms linked to the components of AMOC variability that we have identified. Without sensitivity experiments, it is difficult to separate the relative roles of surface buoyancy forcing and wind forcing in driving AMOC variability since the two are intrinsically coupled (Williams et al. 2014). Thus, in this study, we do not aim to answer how AMOC

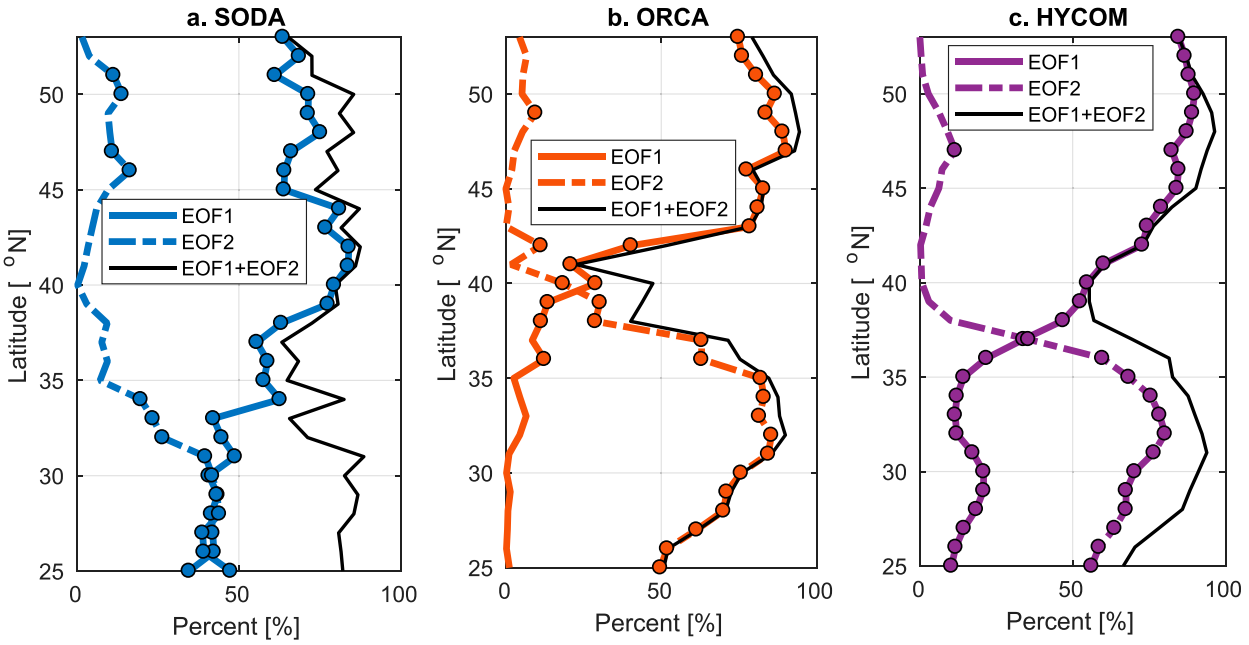


FIG. 5. Contribution of each component to the total AMOC variability at each latitude in (a) SODA, (b) ORCA, and (c) HYCOM. Colored solid (dashed) lines represent the contribution (%) of EOF1 (EOF2) mode to AMOC variability. Black solid lines represent the contribution from the sum of EOF1 and EOF2 modes. Colored circles represent where the contributions (correlations) are significant at 95% confidence level.

variability is dynamically driven. Instead, we focus on the correspondence between AMOC variability and forcing changes, and whether that correspondence is model dependent.

### 1) NAO-RELATED WIND FORCING AND THE GYRE-OPPOSING AMOC VARIABILITY

The time-mean states of wind stress and wind stress curl (WSC) over the North Atlantic are shown in Fig. 6a. (Note that we use the wind field from HYCOM for this plot, but wind field from the other two models yields similar results). The wind stress field in the subtropical region, dominated by easterlies south of 30°N and westerlies north of this latitude, is marked by a strong negative WSC (i.e., clockwise) near 30°N (black box). At ~40°N, there is a positive WSC concentrated near the western boundary (red dashed box). East of the Flemish Cap between 40° and 50°N, where the westerlies are strongest in strength, the WSC is quite small. North of 50°N, positive WSC dominates.

Variability in the wind stress field is revealed by its EOF modes. Figures 7a–c show the first EOF mode

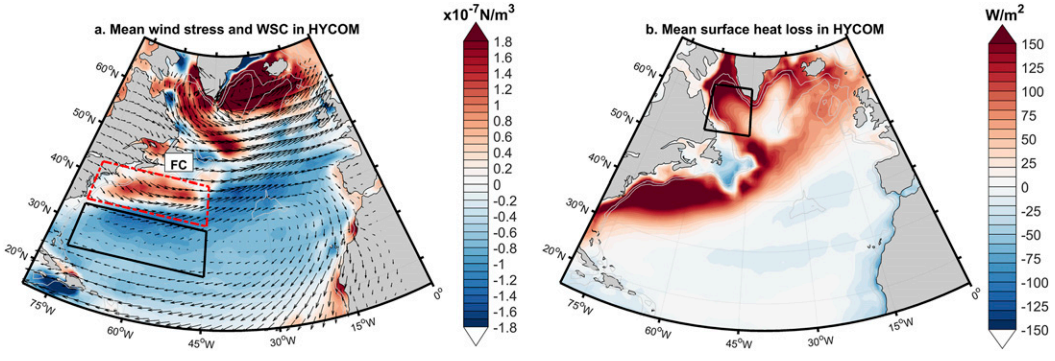


FIG. 6. (a) The mean wind stress field (arrows) and WSC (color shading) in HYCOM. The red dashed box denotes the positive (cyclonic) WSC that centered at 40°N and the black box indicates the negative (anticyclonic) WSC at 30°N in the subtropical region. FC denotes the Flemish Cap. (b) The mean surface heat loss (i.e., positive is heat flux from the ocean to the atmosphere) in HYCOM, with the black box showing the Labrador Sea region.

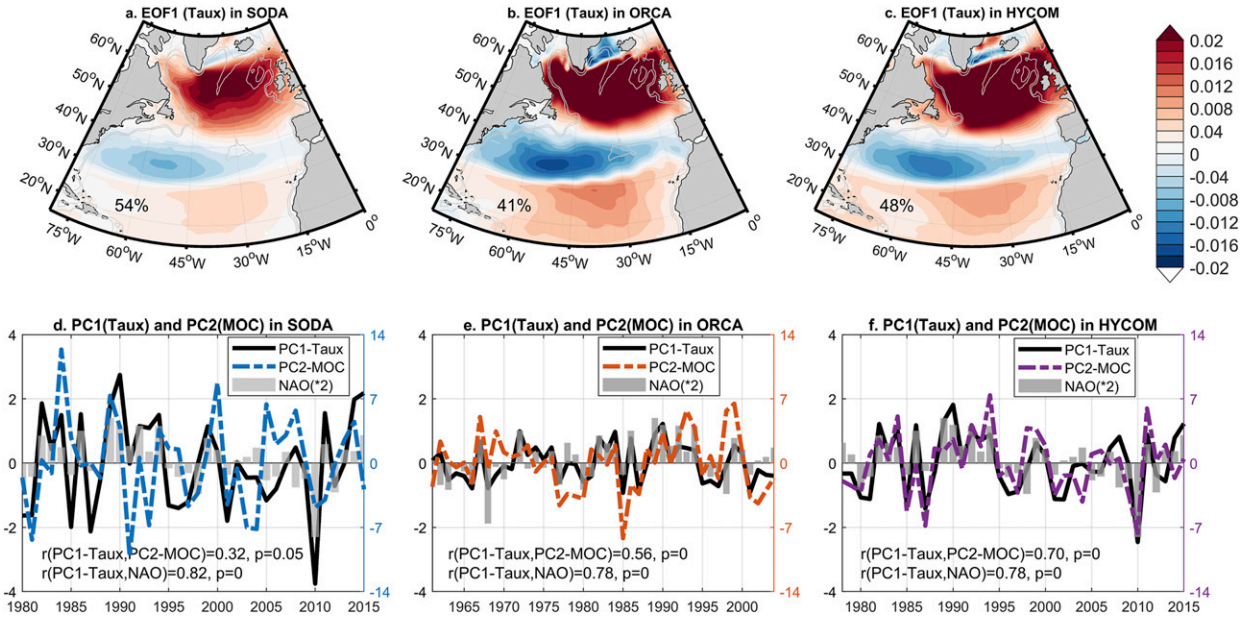


FIG. 7. (a)–(c) EOF1 mode of the annual zonal wind stress magnitude over the North Atlantic in (a) SODA, (b) ORCA, and (c) HYCOM. All time series are detrended before applying the EOF analysis. (d)–(f) Corresponding PC1 time series (black solid lines) of the EOF1 mode shown in (a)–(c). Colored dashed lines represent the PC2 time series for the gyre-opposing component of AMOC variability. Annual NAO (×2 for illustrative purposes) is also plotted with light gray bars. NAO data are obtained from the NOAA National Weather Service Climate Prediction Center (http://www.cpc.ncep.noaa.gov). Correlation coefficients and $p$ values are labeled in (d)–(f).

(EOF1; 41%–54%) for the zonal wind stress in each of the three models. We use the zonal component since it dominates the total wind stress variability and well captures the primary WSC variability (see below). Note also that the EOF is applied to the magnitude of the zonal wind stress variability, without consideration of its sign. This EOF1 mode shows a familiar tripole pattern: easterlies south of 30°N and westerlies north of 50°N strengthen or weaken together, while the westerlies between 30–40°N vary in the opposite direction. Not surprisingly, the zonal wind stress PC1 time series is well correlated with the annual NAO index ($r > 0.78$; Figs. 7d–f). We also find that the wind PC1 time series is closely related to the latitudinal movement of the minimum wind stress isopleth near 30°N ($r > 0.80$; Fig. 8) and the movement of the maximum wind stress isopleth east of the Flemish Cap (not shown). Specifically, when these wind stress isopleths shift northward, the NAO tripole pattern intensifies. As has been pointed out by previous studies (e.g., Woollings and Blackburn 2012; Vallis and Gerber 2008; Luo et al. 2007), this relationship highlights the influence of the

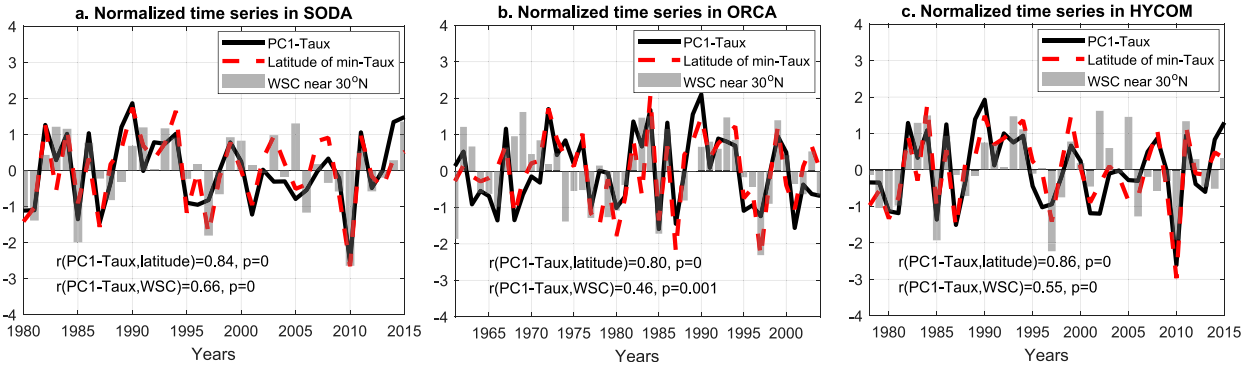


FIG. 8. Time series of the zonal wind stress PC1 (black), the latitude shift of the minimum zonal wind stress in the subtropical region (i.e., in the black box shown in Fig. 6a) (dashed red), and the WSC averaged over the same box (gray bars), in (a) SODA, (b) ORCA, and (c) HYCOM. All time series are detrended and normalized by their standard deviation. All correlation coefficients and their $p$ values are labeled.

North Atlantic jet stream position on local wind stress variability (or NAO phase).

As mentioned earlier, observational and modeling studies have shown that winds are the primary driver of the AMOC variability at subtropical latitudes (e.g., at 26.5°N) (Zhao and Johns 2014; McCarthy et al. 2012). As such, we expect a significant correlation between the wind PC1 and the AMOC PC2 time series, the latter containing most of the subtropical AMOC variability. Figures 7d–f show the expected correlations, especially in ORCA ($r = 0.56$) and HYCOM ($r = 0.70$). In SODA, the correlation, though still significant, is much weaker ($r = 0.32$). The impact of winds on subtropical AMOC variability is twofold. First, strengthened easterlies south of 30°N and weakened westerlies between 30–40°N lead to a stronger AMOC because of positive Ekman transport anomalies in both cases. Second, subtropical AMOC variability can be induced by WSC variability through a response in upper midocean transport. The wind EOF1 mode, which describes the wind stress shear near 30°N, can reflect the local WSC variability: positive wind PC1 is related to increased WSC ($r = 0.66$ in SODA, $r = 0.46$ in ORCA, and $r = 0.55$ in HYCOM; Fig. 8). Specifically, when wind EOF1 mode strengthens, the easterlies south of 30°N increase and westerlies north of 30°N decrease. While the former leads to a negative (i.e., anticyclonic) WSC anomaly and the latter leads to a positive (i.e., cyclonic) WSC anomaly, the magnitude of the easterly increase is overall smaller than that of the westerly decrease, which is evident from the wind EOF1 pattern (Figs. 7a–c). As a result, the WSC anomaly is dominated by decrease of the westerlies north of 30°N and is therefore positive. In addition, the dominant WSC variability over the entire North Atlantic, revealed by its PC1 time series, is significantly linked to the wind PC1 time series ($r = 0.93$ in SODA, $r = 0.86$ in ORCA, $r = 0.62$ in HYCOM; not shown).

Taken together, the interannual AMOC variability in the subtropical gyre is driven by NAO-related wind variability. Specifically, during the positive NAO phase, zonal wind stress strengthens the AMOC through Ekman transport. Meanwhile, the positive WSC anomaly leads to uplifted thermocline anomaly that propagates to the western boundary via planetary waves, where it weakens the cross-basin thermocline tilt, reduces the southward midocean transport, and enhances AMOC strength (Zhao and Johns 2014).

#### 2) Wind forcing at transition latitudes and the meridionally coherent AMOC component on interannual time scales

We further examine AMOC forcing mechanisms by segregating the meridionally coherent AMOC variability according to time scales. Specifically, we filter the AMOC PC1 with a fifth-order Butterworth filter using a cutoff period of 3 years to separate interannual variability (a cutoff period of 5 years yields similar results). The high-pass-filtered time series are considered the interannual component of AMOC PC1, and the remaining time series are considered the semidecadal to decadal component of AMOC PC1.

The interannual AMOC PC1 shows a significant correlation with zonal wind stress variability between 40° and 50°N east of the Flemish Cap, which is the second most dominant mode (i.e., EOF2) of the North Atlantic zonal wind stress (Fig. 9). The wind EOF2 mode, unlike the EOF1 mode, is not associated with the latitudinal shift of the local wind stress maximum, but is instead dominated by the magnitude of the local maximum. The response of interannual AMOC PC1 to wind strength at these latitudes is primarily through Ekman transport (Figs. 9d–f): weakened westerlies reduce the southward Ekman transport and lead to stronger AMOC. The averaged Ekman transport between 40° and 50°N explains 30%–44% of the interannual AMOC PC1 variability (the percentage is calculated as $r^2 \times 100\%$, where $r$ is the correlation coefficient between averaged Ekman transport and interannual AMOC PC1). More specifically, at each latitude between 40° and 50°N, the Ekman transport's contribution to the local interannual AMOC variability ranges from 45% to 75%. Based on a preliminary examination of the longitude-dependent geostrophic transport, the remaining AMOC (i.e., AMOC minus Ekman transport) variability is more related to the geostrophic transport variability east of the Mid-Atlantic Ridge than west of the ridge. The specific process involved remains to be investigated.

#### 3) Cumulative NAO events and the meridionally coherent component for AMOC variability on longer time scales

The low-pass-filtered AMOC PC1, denoting the coherent AMOC variability on semidecadal to decadal time scales, is dominated by the geostrophic component (i.e., the Ekman component is filtered out). Previous studies have shown that the decadal geostrophic component is modulated by the buoyancy difference between the western and eastern boundaries through the thermal wind relation, with a larger contribution from the western boundary (Tulloch and Marshall 2012; Buckley et al. 2012; Buckley and Marshall 2016, and references therein). As stated in the introduction, many modeling studies suggest that the buoyancy anomalies along the

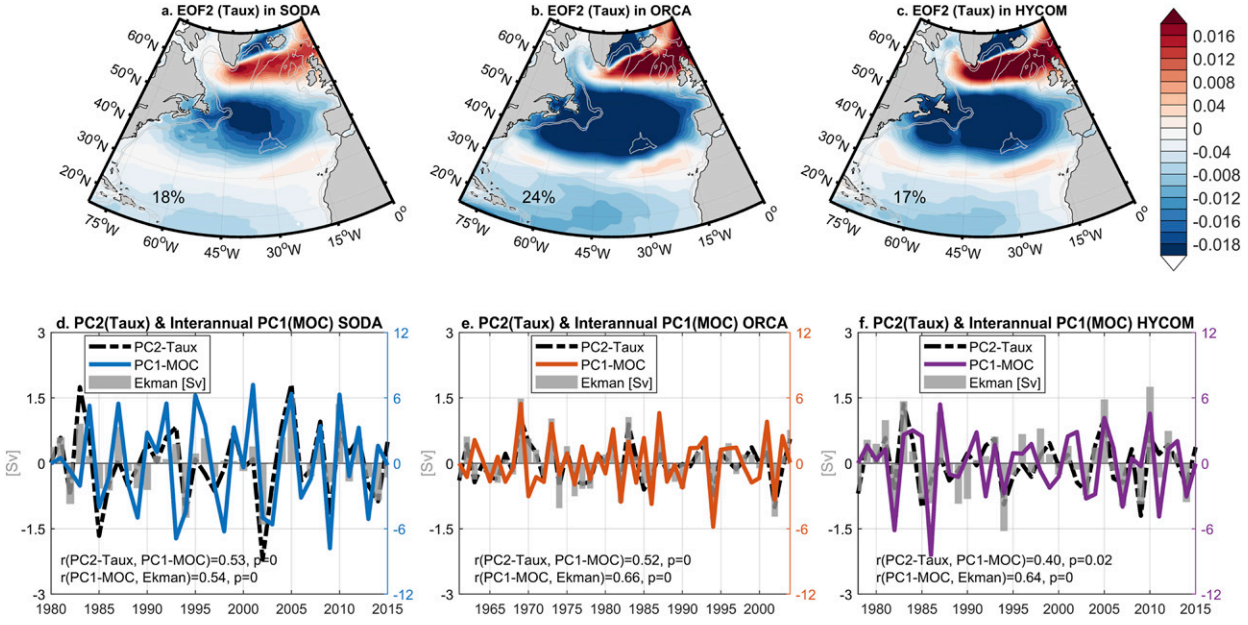


FIG. 9. (a)–(c) EOF2 mode of the annual zonal wind stress over the North Atlantic in (a) SODA, (b) ORCA, and (c) HYCOM. (d)–(f) Corresponding PC2 time series (black dashed lines) of the EOF2 mode shown in (a)–(c). The colored solid lines represent the high-pass-filtered component of the PC1 time series for AMOC (i.e., the high-frequency variability of the meridionally coherent AMOC). The detrended Ekman transport averaged over 40°–50°N is plotted in gray bars. Correlation coefficients and *p* values are labeled in (d)–(f).

western boundary primarily originate from the Labrador Sea (e.g., Yeager and Danabasoglu 2014; Biastoch et al. 2008). Figure 10 shows the comparison between the low-pass-filtered surface heat loss variability (which dominates surface buoyancy flux) over the Labrador Sea (solid black box in Fig. 6b) and the low-pass-filtered AMOC PC1. The correlation between these two time series is model dependent: significant correlations are found in SODA ($r = 0.59$) and HYCOM ($r = 0.60$), with the AMOC PC1 lagging Labrador Sea heat loss by 3 years in SODA and by 1 year in HYCOM; the lagged (5-yr lag) correlation is weak and insignificant ($p$ value = 0.22) in ORCA. The low correlation in ORCA suggests that heat loss in the Labrador Sea alone is not able to explain the low-frequency AMOC variability in this model. Heat loss in

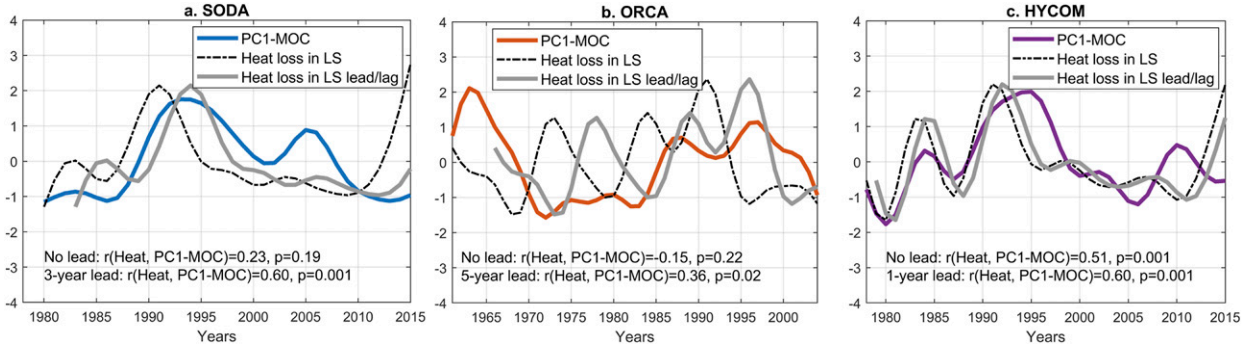


FIG. 10. (a) Low-pass-filtered time series of AMOC PC1 (solid colored line) and low-pass-filtered heat loss in the Labrador Sea (dashed black) in SODA. The Labrador Sea region (53°–62°N, 60°–45°W) over which the heat loss is averaged is shown as a black box in Fig. 6b. The solid gray line shows the heat loss time series that are shifted forward in time by 3 years, which results in the strongest cross-correlation between the two time series. (b) As in (a), but in ORCA. The solid gray line shows the heat loss time series are shifted forward in time by 5 years. (c) As in (a), but in HYCOM. The solid gray line shows the heat loss time series are shifted forward in time by 1 year. For illustration, all time series have been normalized by their standard deviation. In all panels, the correlations and *p* values with and without lead/lag are labeled.

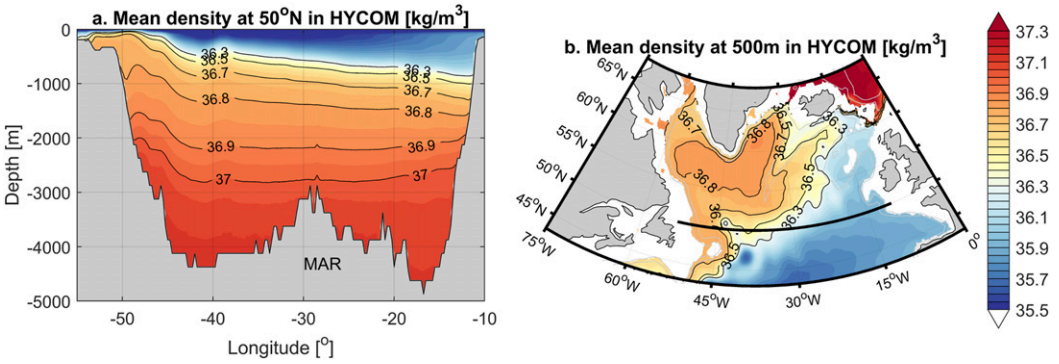


FIG. 11. Spatial distribution of the modeled time-mean density in HYCOM (1978–2015). (a) The vertical distribution along 50°N. (b) The horizontal distribution at 500 m in the subpolar region. The 1000- and 2000-m isobaths are shown in gray. The 50°N section is indicated as a black line. The time-mean density distributions in SODA and ORCA are overall similar to those in HYCOM, except that the density is overall larger in ORCA. Density is referenced to 2000 dbar.

other areas of the subpolar gyre and/or changes in winds may also impact the AMOC strength.

As stated above, the decadal AMOC strength is linked to the zonal density gradient through the thermal wind relation. The density structure at 50°N in HYCOM is shown in Fig. 11a as an example. Density is overall larger along the western boundary and decreases toward the interior and eastern basin, leading to a strong negative zonal density gradient. The gradient is strongest in the upper ~1000 m and weakens with depth. The denser waters along the western boundary originate from the western subpolar gyre, while the lighter waters in the interior/eastern basin travel from the subtropical region (Fig. 11b).

To examine how the zonal density gradient is related to AMOC decadal variability, we compute the density anomalies in the subpolar region (where the decadal AMOC mode is strong) during the decade that is associated with strong/weak AMOC. In HYCOM, during 1989–99 when the AMOC is strong (Fig. 10c), the zonal density difference is enhanced (i.e., more negative eastward): at 50°N in the upper 500 m, the density anomalies are positive along the western boundary ($+0.06\,\mathrm{kg\,m^{-3}}$), strongly negative and surface-intensified in the basin interior away from the western boundary ($-0.08\,\mathrm{kg\,m^{-3}}$), and weakly negative near the eastern boundary ($-0.02\,\mathrm{kg\,m^{-3}}$; east of ~20°W) (Figs. 12a,b). The positive density anomalies along the western boundary start to develop in the early 1990s (see Fig. S1b in the online supplemental material) when AMOC starts to increase (Fig. 10c). In the mid-1990s, the western boundary positive density anomalies reach a maximum (Fig. S1c), resulting in the strongest AMOC. Meanwhile, significant negative density anomalies are present in the basin interior due to the enhanced northward transport of warm waters. The density anomalies near the eastern boundary remain minimal. In the late 1990s, the western boundary density decreases and AMOC weakens (Fig. S1d). During decades with weak AMOC strength (i.e., 1978–88 and 2000–15), the zonal density gradients are reduced due to the negative density anomalies along the western boundary (Fig. S2). These results show that in HYCOM, decadal density gradient changes, which reflect decadal AMOC changes, are dominated by density anomalies along the western boundary with a possible origin from the western subpolar region.

The results in SODA are quite similar to those in HYCOM and are therefore not shown. The results for ORCA, however, are different in that the density anomalies near the eastern boundary are comparable or even stronger than those along the western boundary (Figs. 12c,d). For example, during 1992–2001 when AMOC is strong, the positive density anomalies along the western boundary ($+0.02\,\mathrm{kg\,m^{-3}}$) are smaller in magnitude than the negative density anomalies ($-0.04\,\mathrm{kg\,m^{-3}}$) near the eastern boundary. The positive density anomalies start to develop in the early 1990s ($+0.04\,\mathrm{kg\,m^{-3}}$ at 500 m; Fig. S3b) when AMOC increases, similar to that in HYCOM. However, in the mid-1990s, when AMOC is the strongest during the decade, the positive density anomalies along the western boundary are quite weak ($+0.02\,\mathrm{kg\,m^{-3}}$ at 500 m; Fig. S3c). Instead, stronger negative density anomalies are present near the eastern boundary ($-0.04\,\mathrm{kg\,m^{-3}}$), which is likely attributed to the eastward extension of the North Atlantic Current (NAC) which carries warm waters northward. The eastern boundary dominated density structure also applies to the other strong AMOC decade (1961–68) and the weak AMOC decade (1969–85) in ORCA (Fig. S4).

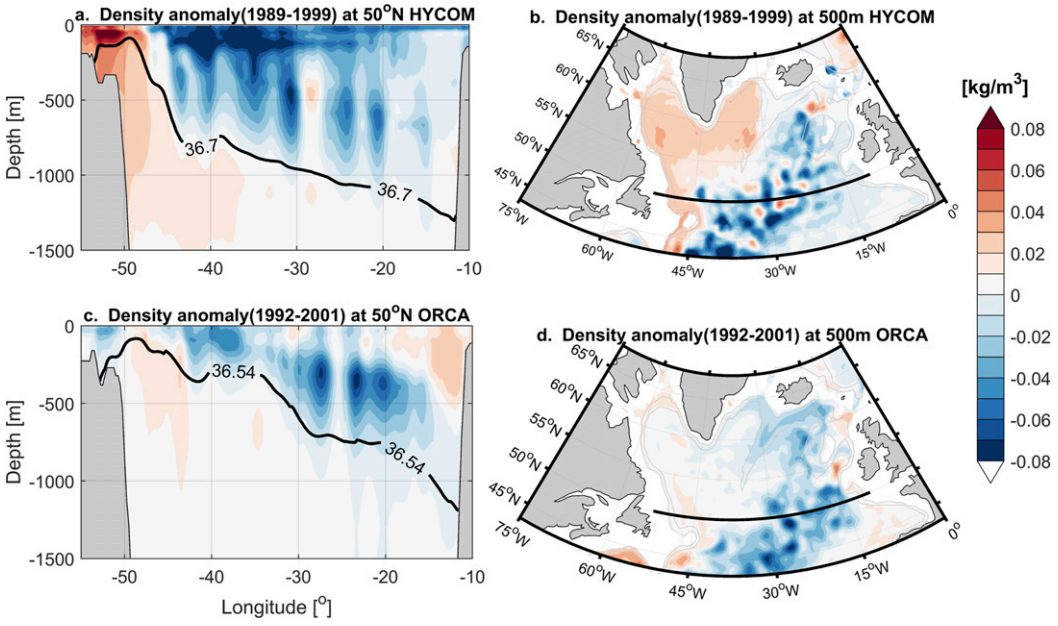


FIG. 12. (a) Density anomalies in the upper 1500 m across 50°N during 1989–99 in HYCOM. This decade is characterized by a strong AMOC strength (Fig. 10c). The climatological isopycnal of 36.70 kg $m^{-3}$, where the mean AMOC is reached at 50°N, is contoured in black for reference. (b) Density anomalies at 500 m during the same period in HYCOM. The 50°N section is shown as a black line; 1000- and 2000-m isobaths are shown in gray. (c) Density anomalies in the upper 1500 m across 50°N during 1992–2001 in ORCA, when the decadal AMOC is strong (Fig. 10b). Climatological isopycnal of 36.54 kg $m^{-3}$, where the mean AMOC is reached at 50°N, is contoured in black. (d) Density anomalies at 500 m during the same period in ORCA. Density is referenced to 2000 dbar.

The anomalies of surface heat loss and zonal wind stress during strong (weak) AMOC decade are shown in Figs. 13a and 13b (Fig. S5) for HYCOM. When decadal AMOC is strong (weak), there is an enhanced (reduced) surface heat loss in the Labrador Sea and along the western boundary, coupled with strengthened (weakened) westerlies. This is consistent with previous modeling studies showing that western boundary density anomalies are related to the surface buoyancy/heat flux in the Labrador Sea (e.g., Biastoch et al. 2008). There are also significant decadal changes of heat loss and wind stress in the Iceland basin, possibly modifying water mass transformation in that basin. The decadal changes of heat loss and wind stress in SODA and ORCA are similar to those in HYCOM, except that these changes are not completely in phase with AMOC changes. This is especially true for ORCA, where surface heat loss in the Labrador Sea leads decadal AMOC variability by 5 years (Fig. 10b). As a result, we compare the anomalies of heat loss and wind stress 5 years before the strong/weak AMOC time period in ORCA. The anomaly patterns are very similar to those in HYCOM (Figs. 13c,d; Fig. S6): 5 years prior to a strong (weak) AMOC, surface heat loss and the westerlies are enhanced (reduced) in the Labrador Sea, along the western boundary current and in the Iceland basin. However, the readers are reminded that though there is a lagged correspondence between AMOC strength and the surface heat loss in ORCA, the correlation between the two is as low as 0.36 (Fig. 10b) and the role of the density anomalies along the western boundary is not pivotal.

In summary, in all three models, the decadal variability contained in AMOC PC1 is associated with cross-basin density gradient in the subpolar region. In HYCOM and SODA, the density gradient is dominated by density anomalies along the western boundary, with an origin from the western subpolar gyre where surface heat loss and westerlies exhibit significant decadal variability. This is consistent with the findings in Tulloch and Marshall (2012) and Buckley et al. (2012). In ORCA, however, density anomalies on both sides of the basin are important. While the origin of the western boundary anomalies in ORCA is similar to that in HYCOM and SODA, the mechanism that controls the density anomalies near the eastern boundary is not investigated here, although we do see an impact from the eastward extension of the NAC.

Finally, despite the model differences discussed above (especially the difference between ORCA and the other

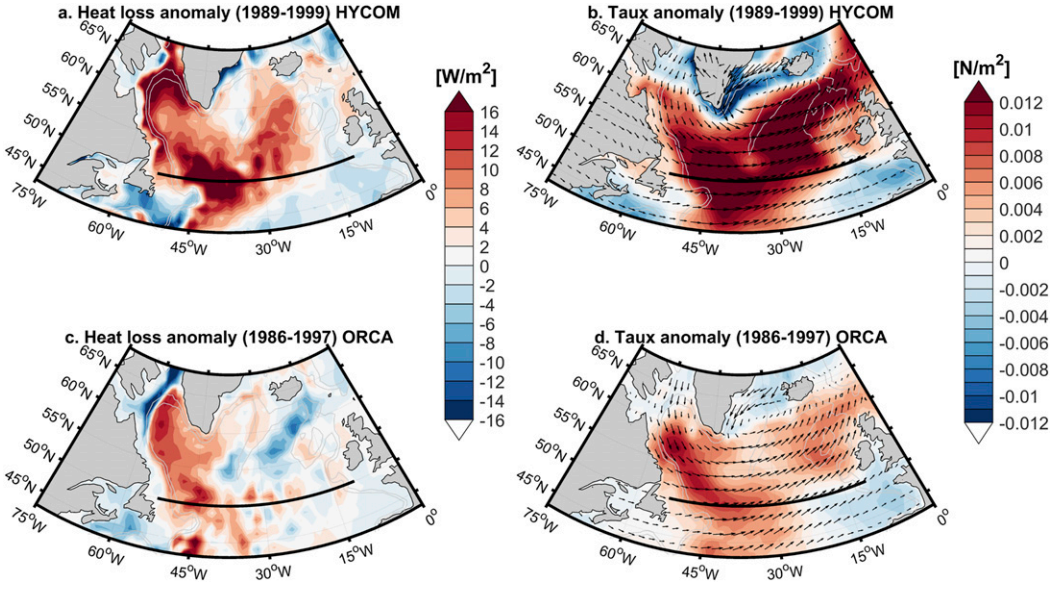


FIG. 13. (a) Surface heat loss anomalies during a period of strong decadal AMOC (1989–99) in HYCOM. Positive values indicate more heat loss from ocean to the atmosphere. The 50°N section is shown as a black line. (b) Zonal wind stress magnitude anomalies during the same period. Positive values indicate stronger zonal wind stress without considering its sign. The climatological zonal and meridional wind stress fields are shown with black arrows for reference. (c) Surface heat loss anomalies during 1986–97 in ORCA. This time period is 5 years before the strong decadal AMOC takes place (1991–2002). (d) Zonal wind stress magnitude anomalies during the same period in (c). The climatological zonal and meridional wind stress fields are shown with black arrows for reference.

two models), we find that the low-frequency AMOC variability is strongly related to the cumulative NAO index in all models ($r$ = 0.93 in SODA; $r$ = 0.75 in ORCA; $r$ = 0.6 in HYCOM; Fig. 14). This suggests that persistent NAO conditions, which include both continuous heat loss/gain and persistently strong/weak winds, are better indicators of the low-frequency AMOC variability compared to individual NAO events (or individual surface heat flux events as shown in Fig. 10). This is especially true for ORCA, where the correlation between Labrador Sea heat loss (linked to annual NAO index) and low-frequency AMOC PC1 is insignificant even with lags (Fig. 10b). Similar cumulative effects have been reported by previous studies. For example, Robson et al. (2012) showed that the rapid warming of the subpolar North Atlantic in the 1990s was associated with "prolonged positive phase of the NAO" and changes in the AMOC, instead of with individual NAO events.

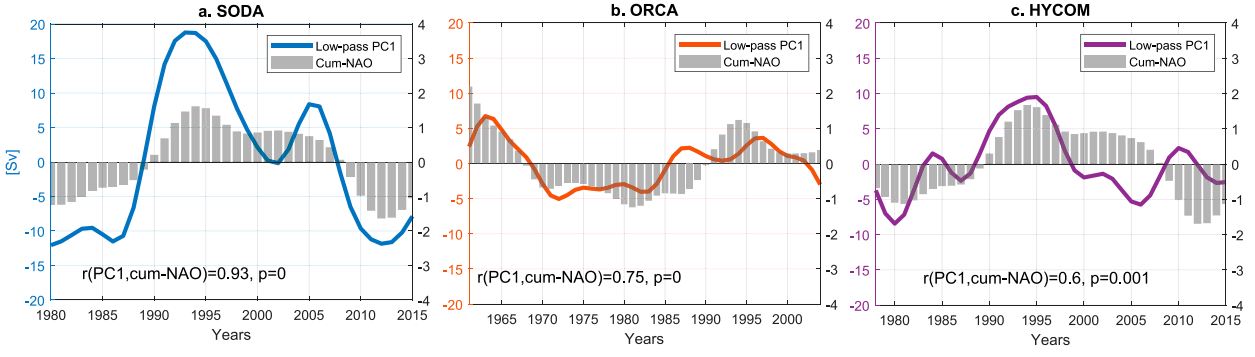


FIG. 14. (a) Low-pass-filtered time series of AMOC PC1 (blue) and cumulative NAO index (light gray bars) in SODA. The cumulative NAO index is calculated by integrating the annual NAO index from 1950 and onward, and is detrended over the model's temporal span (i.e., 1980–2015). (b) As in (a), but in ORCA with the cumulative NAO time series detrended over 1961–2004. (c) As in (a), but in HYCOM with cumulative NAO time series detrended over 1978–2015. The correlations and $p$ values are labeled in all panels.

## 4. Conclusions

Motivated by previous studies that have depicted the AMOC as a meridionally coherent feature driven by high-latitude buoyancy forcing and disturbed by local wind forcing, this study re-examines the meridional structure of AMOC variability and diagnoses the associated forcing scenarios with three different models.

From our decomposition of AMOC variability into meridionally coherent and gyre-opposing modes, we find that AMOC variability north of 40°N is mostly explained by the former, with a small contribution from the latter. At specific latitudes (40°–43°N), the gyre-opposing mode is zero and AMOC variability is only dependent on the meridionally coherent mode. In contrast, AMOC variability in the subtropical region is mostly contained in the gyre-opposing mode in ORCA and HYCOM. In SODA, both the meridionally coherent mode and the gyre-opposing mode contribute significantly to the subtropical AMOC variability. We further highlight the special role of the transition latitudes, which not only connect the coherent AMOC signal between the subpolar and the subtropical latitudes, but also serve as a boundary separating gyre-localized AMOC variability, similar to previous studies (e.g., Bingham et al. 2007; Xu et al. 2014).

The meridionally coherent AMOC variability is further discussed based on time scales. On decadal time scales, AMOC variability is linked to the zonal density difference between the western and the eastern boundaries. The zonal density difference is dominated by density anomalies along the western boundary in SODA and HYCOM, which originate from the western subpolar region under significant decadal surface heat flux and wind variability. In ORCA, on the other hand, density anomalies on both boundaries are important. While western boundary density anomalies exhibit similar origin from the western subpolar region, the eastern boundary density anomalies appear to be impacted by the eastward extension of the NAC. Further investigation is needed to understand the density structure along the eastern boundary. Despite these differences, all models show significant linkage between decadal AMOC variability and the cumulative NAO index, the latter corresponding to persistent NAO conditions. On interannual time scales, all models show that the AMOC variability contained in the meridionally coherent mode is linked to the strength of the westerlies between 40° and 50°N through a significant response in Ekman transport. Finally, the gyre-opposing AMOC mode, dominated by interannual variability, is shown to respond to the NAO-related winds in the subtropical region (south of 40°N). This is consistent in all models.

Recent observations, albeit of limited duration, show that the strong convection in the Labrador Sea due to enhanced surface buoyancy flux during 2014–15 did not translate to a strong AMOC, questioning the linkage between the two processes (Lozier et al. 2019). Using observational and reanalysis data from the 1990s to the present, a follow-on study by Zou et al. (2020) attributes the weak linkage between Labrador Sea convection and AMOC strength to strong density compensation in the boundary current of the Labrador Sea. Thus, these findings suggest that density anomalies along the western boundary of the subpolar North Atlantic cannot be assumed to be a product of Labrador Sea convection. The question is why SODA and HYCOM show a strong correspondence among Labrador Sea heat loss, western boundary density anomalies, and the AMOC strength.

One possible answer is that the compensated density structure that is observed in the Labrador Sea is not well represented in SODA and HYCOM and, as a result, modeled density anomalies from the convective region propagate southward along the western boundary and modify the AMOC strength. For example, due to a known salinity bias in the Labrador Sea, the overturning strength within the Labrador Sea in HYCOM is ~10 Sv (Xu et al. 2018b), much stronger than the observed value of 2 Sv (Lozier et al. 2019). Another possibility is that while the western boundary density anomalies show apparent correspondence with the Labrador Sea buoyancy loss (or convection), the two are not dynamically related. For example, the density anomalies may be generated in the Iceland and/or Irminger basins and then propagate westward to the Labrador Sea or to the western boundary as topographic Rossby waves. It is also possible that the density anomalies are generated locally within the western boundary current, where significant surface heat loss and wind stress changes are present (Fig. 13).

Diapycnal transformation along the boundary current in the western subpolar gyre, as well as that in the Iceland basin (Xu et al. 2018b; Desbruyères et al. 2019), in response to significant decadal surface heat loss (Fig. 13), may play an important role in determining decadal AMOC variability. In addition, winds can also create/enhance AMOC coherence on interannual to decadal time scales. For example, a recent modeling study shows that subtropical AMOC variability can be remotely forced by wind stress anomalies at midlatitudes through mass imbalance adjustment (Spall and Nieves 2019).

Finally, we note that the results presented in this study are based on ocean reanalysis and eddy-resolving/eddy-permitting ocean circulation models, which have been

shown to represent some of the key circulation features in the North Atlantic (e.g., Xu et al. 2013, 2018a for HYCOM; Gary et al. (2011) and Zou and Lozier (2016) for ORCA; Carton et al. 2018 for SODA). Due to different model formulation, resolution, atmospheric forcing products, and inclusion of data assimilation or not, there are significant differences in the time mean and the variability of the AMOC. The consistent pattern in the meridional structure of AMOC variability in these models implies that the findings presented here are robust.

*Acknowledgments.* The authors gratefully acknowledge support from the Physical Oceanography Program of the U.S. National Science Foundation (Awards OCE-1756143 and OCE-1537136) and the Climate Program Office of the National Oceanic and Atmospheric Administration (Award NA15OAR4310088). Gratitude is extended to Claus Böning and Arne Biastoch who shared ORCA025 output. S. Zou thanks F. Li, M. Buckley, and L. Li for helpful discussions. We also thank three anonymous reviewers for helpful suggestions.

Data availability statement: SODA3.4.2 is available at http://www.atmos.umd.edu/~ocean/. ORCA025 outputs are obtained from C. Böning and A. Biastoch at GEOMAR–Helmholtz-Zentrum für Ozeanforschung Kiel. HYCOM model outputs can be accessed on request to X.X. The NAO index is downloaded from NOAA Climate Prediction Center at http://www.cpc.ncep.noaa.gov.

## REFERENCES

Barnier, B., and Coauthors, 2006: Impact of partial steps and momentum advection schemes in a global ocean circulation model at eddy permitting resolution. *Ocean Dyn.*, **56**, 543–567, https://doi.org/10.1007/s10236-006-0082-1.

——, and Coauthors, 2007: Eddy-permitting ocean circulation hindcasts of past decades. *CLIVAR Exchanges*, No. 42, International CLIVAR Project Office, Southampton, United Kingdom, 8–10.

Biastoch, A., C. W. Böning, J. Getzlaff, J. M. Molines, and G. Madec, 2008: Causes of interannual–decadal variability in the meridional overturning circulation of the midlatitude North Atlantic Ocean. *J. Climate*, **21**, 6599–6615, https://doi.org/10.1175/2008JCLI2404.1.

Bingham, R. J., C. W. Hughes, V. Roussenov, and R. G. Williams, 2007: Meridional coherence of the North Atlantic meridional overturning circulation. *Geophys. Res. Lett.*, **34**, L23606, https://doi.org/10.1029/2007GL031731.

Böning, C. W., M. Scheinert, J. Dengg, A. Biastoch, and A. Funk, 2006: Decadal variability of subpolar gyre transport and its reverberation in the North Atlantic overturning. *Geophys. Res. Lett.*, **33**, L21S01, https://doi.org/10.1029/2006GL026906.

Buckley, M. W., and J. Marshall, 2016: Observations, inferences, and mechanisms of the Atlantic Meridional Overturning Circulation: A review. *Rev. Geophys.*, **54**, 5–63, https://doi.org/10.1002/2015RG000493.

——, D. Ferreira, J. M. Campin, J. Marshall, and R. Tulloch, 2012: On the relationship between decadal buoyancy anomalies and variability of the Atlantic meridional overturning circulation. *J. Climate*, **25**, 8009–8030, https://doi.org/10.1175/JCLI-D-11-00505.1.

Cabanes, C., T. Lee, and L. L. Fu, 2008: Mechanisms of interannual variations of the meridional overturning circulation of the North Atlantic Ocean. *J. Phys. Oceanogr.*, **38**, 467–480, https://doi.org/10.1175/2007JPO3726.1.

Carton, J. A., and B. S. Giese, 2008: A reanalysis of ocean climate using Simple Ocean Data Assimilation (SODA). *Mon. Wea. Rev.*, **136**, 2999–3017, https://doi.org/10.1175/2007MWR1978.1.

——, G. A. Chepurin, and L. Chen, 2018: SODA3: A new ocean climate reanalysis. *J. Climate*, **31**, 6967–6983, https://doi.org/10.1175/JCLI-D-18-0149.1.

Danabasoglu, G., S. G. Yeager, Y. O. Kwon, J. J. Tribbia, A. S. Phillips, and J. W. Hurrell, 2012: Variability of the Atlantic meridional overturning circulation in CCSM4. *J. Climate*, **25**, 5153–5172, https://doi.org/10.1175/JCLI-D-11-00463.1.

Delworth, T., S. Manabe, and R. J. Stouffer, 1993: Interdecadal variations of the thermohaline circulation in a coupled ocean–atmosphere model. *J. Climate*, **6**, 1993–2011, https://doi.org/10.1175/1520-0442(1993)006<1993:IVOTTC>2.0.CO;2.

Desbruyères, D. G., H. Mercier, G. Maze, and N. Daniault, 2019: Surface predictor of overturning circulation and heat content change in the subpolar North Atlantic. *Ocean Sci.*, **15**, 809–817, https://doi.org/10.5194/os-15-809-2019.

Eden, C., and J. Willebrand, 2001: Mechanism of interannual to decadal variability of the North Atlantic circulation. *J. Climate*, **14**, 2266–2280, https://doi.org/10.1175/1520-0442(2001)014<2266:MOITDV>2.0.CO;2.

Elipot, S., E. Frajka-Williams, C. W. Hughes, S. Olhede, and M. Lankhorst, 2017: Observed basin-scale response of the North Atlantic meridional overturning circulation to wind stress forcing. *J. Climate*, **30**, 2029–2054, https://doi.org/10.1175/JCLI-D-16-0664.1.

Gary, S. F., M. S. Lozier, C. W. Böning, and A. Biastoch, 2011: Deciphering the pathways for the deep limb of the meridional overturning circulation. *Deep-Sea Res. II*, **58**, 1781–1797, https://doi.org/10.1016/j.dsr2.2010.10.059.

Getzlaff, J., C. W. Böning, C. Eden, and A. Biastoch, 2005: Signal propagation related to the North Atlantic overturning. *Geophys. Res. Lett.*, **32**, L09602, https://doi.org/10.1029/2004GL021002.

Goosse, H., 1997: Modeling the large scale behaviour of the coupled ocean–sea ice system. Ph.D. thesis, Université Catholique de Louvain, 231 pp.

Häkkinen, S., 1999: Variability of the simulated meridional heat transport in the North Atlantic for the period 1951–1993. *J. Geophys. Res.*, **104**, 10 991–11 007, https://doi.org/10.1029/1999JC900034.

Johnson, H. L., and D. P. Marshall, 2002: A theory for the surface Atlantic response to thermohaline variability. *J. Phys. Oceanogr.*, **32**, 1121–1132, https://doi.org/10.1175/1520-0485(2002)032<1121:ATFTSA>2.0.CO;2.

Kelly, K. A., L. Thompson, and J. Lyman, 2014: The coherence and impact of meridional heat transport anomalies in the Atlantic Ocean inferred from observations. *J. Climate*, **27**, 1469–1487, https://doi.org/10.1175/JCLI-D-12-00131.1.

Li, F., M. S. Lozier, G. Danabasoglu, N. P. Holliday, Y. O. Kwon, A. Romanou, S. G. Yeager, and R. Zhang, 2019: Local and downstream relationships between Labrador Sea Water volume and North Atlantic meridional overturning circulation variability. *J. Climate*, **32**, 3883–3898, https://doi.org/10.1175/JCLI-D-18-0735.1.

Little, C. M., C. G. Piecuch, and R. M. Ponte, 2017: On the relationship between the meridional overturning circulation, alongshore wind stress, and United States East Coast sea level in the Community Earth System Model Large Ensemble. *J. Geophys. Res. Oceans*, **122**, 4554–4568, https://doi.org/10.1002/2017JC012713.

Lozier, M. S., V. Roussenov, M. S. Reed, and R. G. Williams, 2010: Opposing decadal changes for the North Atlantic meridional overturning circulation. *Nat. Geosci.*, **3**, 728–734, https://doi.org/10.1038/ngeo947.

——, and Coauthors, 2019: A sea change in our view of overturning in the subpolar North Atlantic. *Science*, **363**, 516–521, https://doi.org/10.1126/science.aau6592.

Luo, D., T. Gong, and Y. Diao, 2007: Dynamics of eddy-driven low-frequency dipole modes. Part III: Meridional displacement of westerly jet anomalies during two phases of NAO. *J. Atmos. Sci.*, **64**, 3232–3248, https://doi.org/10.1175/JAS3998.1.

Marotzke, J., and B. A. Klinger, 2000: The dynamics of equatorially asymmetric thermohaline circulations. *J. Phys. Oceanogr.*, **30**, 955–970, https://doi.org/10.1175/1520-0485(2000)030<0955:TDOEAT>2.0.CO;2.

Marshall, D. P., and H. L. Johnson, 2013: Propagation of meridional circulation anomalies along western and eastern boundaries. *J. Phys. Oceanogr.*, **43**, 2699–2717, https://doi.org/10.1175/JPO-D-13-0134.1.

McCarthy, G., and Coauthors, 2012: Observed interannual variability of the Atlantic meridional overturning circulation at 26.5°N. *Geophys. Res. Lett.*, **39**, L19609, https://doi.org/10.1029/2012GL052933.

Pardaens, A. K., J. M. Gregory, and J. A. Lowe, 2011: A model study of factors influencing projected changes in regional sea level over the twenty-first century. *Climate Dyn.*, **36**, 2015–2033, https://doi.org/10.1007/s00382-009-0738-x.

Pickart, R. S., and M. A. Spall, 2007: Impact of Labrador Sea convection on the North Atlantic meridional overturning circulation. *J. Phys. Oceanogr.*, **37**, 2207–2227, https://doi.org/10.1175/JPO3178.1.

Polo, I., J. Robson, R. Sutton, and M. A. Balmaseda, 2014: The importance of wind and buoyancy forcing for the boundary density variations and the geostrophic component of the AMOC at 26°N. *J. Phys. Oceanogr.*, **44**, 2387–2408, https://doi.org/10.1175/JPO-D-13-0264.1.

Robson, J., R. Sutton, K. Lohmann, D. Smith, and M. D. Palmer, 2012: Causes of the rapid warming of the North Atlantic Ocean in the mid-1990s. *J. Climate*, **25**, 4116–4134, https://doi.org/10.1175/JCLI-D-11-00443.1.

——, P. Ortega, and R. Sutton, 2016: A reversal of climatic trends in the North Atlantic since 2005. *Nat. Geosci.*, **9**, 513–517, https://doi.org/10.1038/ngeo2727.

Rosmond, T., J. Teixeira, M. Peng, T. Hogan, and R. Pauley, 2002: Navy operational global atmospheric prediction system (NOGAPS): Forcing for ocean models. *Oceanography*, **15**, 99–108, https://doi.org/10.5670/oceanog.2002.40.

Spall, M. A., and D. Nieves, 2019: Wind-forced variability of the remote meridional overturning circulation. *J. Phys. Oceanogr.*, **50**, 455–469, https://doi.org/10.1175/JPO-D-19-0190.1.

Stouffer, R. J., and Coauthors, 2006: Investigating the causes of the response of the thermohaline circulation to past and future climate changes. *J. Climate*, **19**, 1365–1387, https://doi.org/10.1175/JCLI3689.1.

Tulloch, R., and J. Marshall, 2012: Exploring mechanisms of variability and predictability of Atlantic meridional overturning circulation in two coupled climate models. *J. Climate*, **25**, 4067–4080, https://doi.org/10.1175/JCLI-D-11-00460.1.

Uppala, S. M., and Coauthors, 2005: The ERA-40 Re-Analysis. *Quart. J. Roy. Meteor. Soc.*, **131**, 2961–3012, https://doi.org/10.1256/qj.04.176.

Vallis, G. K., and E. P. Gerber, 2008: Local and hemispheric dynamics of the North Atlantic Oscillation, annular patterns and the zonal index. *Dyn. Atmos. Oceans*, **44**, 184–212, https://doi.org/10.1016/j.dynatmoce.2007.04.003.

Williams, R. G., V. Roussenov, D. Smith, and M. S. Lozier, 2014: Decadal evolution of ocean thermal anomalies in the North Atlantic: The effects of Ekman, overturning, and horizontal transport. *J. Climate*, **27**, 698–719, https://doi.org/10.1175/JCLI-D-12-00234.1.

Woollings, T., and M. Blackburn, 2012: The North Atlantic jet stream under climate change and its relation to the NAO and EA patterns. *J. Climate*, **25**, 886–902, https://doi.org/10.1175/JCLI-D-11-00087.1.

Xu, X., H. E. Hurlburt, W. J. Schmitz Jr., J. Fischer, R. Zantopp, and P. J. Hogan, 2013: On the currents and transports connected with the Atlantic meridional overturning circulation in the subpolar North Atlantic. *J. Geophys. Res. Oceans*, **118**, 502–516, https://doi.org/10.1002/jgrc.20065.

——, E. P. Chassignet, W. E. Johns, W. J. Schmitz Jr., and E. J. Metzger, 2014: Intraseasonal to interannual variability of the Atlantic meridional overturning circulation from eddy-resolving simulations and observations. *J. Geophys. Res. Oceans*, **119**, 5140–5159, https://doi.org/10.1002/2014JC009994.

——, P. B. Rhines, and E. P. Chassignet, 2016: Temperature–salinity structure of the North Atlantic circulation and associated heat and freshwater transports. *J. Climate*, **29**, 7723–7742, https://doi.org/10.1175/JCLI-D-15-0798.1.

——, A. Bower, H. Furey, and E. P. Chassignet, 2018a: Variability of the Iceland-Scotland overflow water transport through the Charlie-Gibbs Fracture Zone: Results from an eddying simulation and observations. *J. Geophys. Res. Oceans*, **123**, 5808–5823, https://doi.org/10.1029/2018JC013895.

——, P. B. Rhines, and E. P. Chassignet, 2018b: On mapping the diapycnal water mass transformation of the upper North Atlantic Ocean. *J. Phys. Oceanogr.*, **48**, 2233–2258, https://doi.org/10.1175/JPO-D-17-0223.1.

Yeager, S., and G. Danabasoglu, 2014: The origins of late-twentieth-century variations in the large-scale North Atlantic circulation. *J. Climate*, **27**, 3222–3247, https://doi.org/10.1175/JCLI-D-13-00125.1.

Zhang, R., 2010: Latitudinal dependence of Atlantic Meridional Overturning Circulation (AMOC) variations. *Geophys. Res. Lett.*, **37**, L16703, https://doi.org/10.1029/2010GL044474.

——, and T. L. Delworth, 2006: Impact of Atlantic multidecadal oscillations on India/Sahel rainfall and Atlantic hurricanes. *Geophys. Res. Lett.*, **33**, L17712, https://doi.org/10.1029/2006GL026267.

Zhao, J., 2017: Basinwide response of the Atlantic meridional overturning circulation to interannual wind forcing. *Climate Dyn.*, **49**, 4263–4280, https://doi.org/10.1007/s00382-017-3568-2.

——, and W. Johns, 2014: Wind-forced interannual variability of the Atlantic meridional overturning circulation at 26.5°N. *J. Geophys. Res. Oceans*, **119**, 2403–2419, https://doi.org/10.1002/2013JC009407.

Zou, S., and M. S. Lozier, 2016: Breaking the linkage between Labrador Sea Water production and its advective export to the subtropical gyre. *J. Phys. Oceanogr.*, **46**, 2169–2182, https://doi.org/10.1175/JPO-D-15-0210.1.

——, ——, and M. Buckley, 2019: How is meridional coherence maintained in the lower limb of the Atlantic meridional overturning circulation? *Geophys. Res. Lett.*, **46**, 244–252, https://doi.org/10.1029/2018GL080958.

——, ——, F. Li, R. Abernathey, and L. Jackson, 2020: Density-compensated overturning in the Labrador Sea. *Nat. Geosci.*, **13**, 121–126, https://doi.org/10.1038/S41561-019-0517-1.